2020 IEEE/RSJ International Conference on Intelligent Robots and Systems (IROS)
October 25-29, 2020, Las Vegas, NV, USA (Virtual)

Analysis of Contact Stability and Contact Safety of a Robotic Intravascular Cardiac Catheter under Blood Flow Disturbances

Ran Hao, Nate Lombard Poirot, M. Cenk Çavuşoğlu

***Abstract*— This paper studies the contact stability and contact safety of a robotic intravascular cardiac catheter under blood flow disturbances while in contact with tissue surface. A probabilistic blood flow disturbance model, where the blood flow drag forces on the catheter body are approximated using a quasi-static model, is introduced. Using this blood flow disturbance model, probabilistic contact stability and contact safety metrics, employing a sample based representation of the blood flow velocity distribution, are proposed. Finally, the contact stability and contact safety of a MRI-actuated robotic catheter are analyzed using these models in a specific example scenario under left pulmonary inferior vein (LIV) blood flow disturbances.**

I. Introduction

In the robotic-assisted atrial fibrillation ablation procedure, a robotically controlled intra-cardiac catheter is guided within the left atrium (Fig. 1) to create lesions that would prevent conduction of irregular electrical activities by performing point-by-point radiofrequency ablation [1].

In radiofrequency ablation, the contact force between the catheter tip and the target tissue is critical for effective lesion formation. As the catheter ablation requires point-by-point creation of lesions on the tissue surface, it is crucial for the robotic catheter to maintain a stable contact with desired contact force under blood flow disturbances during the ablation. Specifically, the stable contact ensures no slippage between the catheter-tip and the tissue surface under the blood flow disturbances, and the safe contact ensures a normal contact force within the desired force limits under the blood flow disturbances. While contact force control under surface motion disturbances has been investigated by multiple studies (e.g., [2]–[7]), to the best of our knowledge, contact stability under blood flow disturbances has not been previously studied in the literature.

This paper investigates the contact stability and contact safety of a robotic catheter under blood flow disturbances given tip position constraint on the tissue surface. The MRI-actuated robotic catheter [8], [9] designed for performing intra-vascular cardiac interventions, including circumferential pulmonary vein ablation for treatment of atrial fibrillation, is used as the underlying example robotic catheter platform. In the present study, a pseudo-rigid-body (PRB) model [10], [11] is employed to model the catheter mechanics. The blood flow disturbances are modeled using a probabilistic model, where the blood flow disturbance model approximates the blood flow drag forces on the catheter body using a quasi-static model, assuming the blood flow to be constant and uniform within a small time interval. Using this blood flow disturbance model, probabilistic contact stability and contact safety metrics are introduced, employing a sample based representation of the blood flow velocity distribution. Finally, the contact stability and contact safety of the robotic catheter are analyzed using these models under left pulmonary inferior vein (LIV) blood flow disturbances.

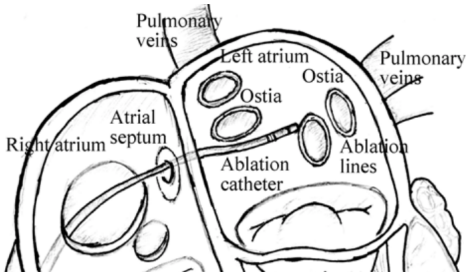

Fig. 1. Illustration of the robotic catheter ablation procedure [8].

The rest of this paper is organized as follows. Related work is presented in Section II. The pseudo-rigid-body model of the robot under surface constraint is reviewed in Section III. The contact model is introduced in Section IV and the probabilistic contact stability and contact safety metrics are introduced in Section V. The simulation based contact stability and safety analysis is presented in Section VI. Conclusions are presented in Section VII.

II. Related Work

As noted by multiple studies, contact force is one of the most important determinants of radiofrequency lesion size [12]–[17]. Adequate contact force must be applied during the ablation procedure to prevent atrial fibrillation recurrence. Reddy et al. [12] suggest that the contact force below 10 g (0.1 N) will cause clinical failure, and the ablation outcome is best achieved with contact force of > 20 g (0.2 N). Andrade et al. [13] show that contact force > 20 g can significantly reduce the rate of arrhythmia recurrence. Wakili et al. [14] show that contact force > 10 g can create more effective lesions. Pedrote et al. [15] suggest that excessive contact force (> 50 g) can provoke steam pop. Thiagalingam et al. [16] indicate that a "moderate" catheter contact force (20 g) can increase the possibility of more effective lesions, and a

This work was supported in part by the National Science Foundation under grants CISE IIS-1524363, CISE IIS-1563805, ENG IIP-1700839, and the National Heart, Lung, and Blood Institute of the National Institutes of Health under grant R01 HL153034.

RH, NLP, and MCC are with the Department of Electrical, Computer, and Systems Engineering, Case Western Reserve University, Cleveland, OH. They can be reached via email at {rxh349,njl49,mcc14}@case.edu respectively.

"high" contact force of 60 g can cause steam pop. Sohns et al. [17] also suggest that contact force of 20 g is recommended and the minimum of 10 g is required.

Dewire and Calkins [18] provide a review of the performance of current ablation techniques and technologies. They conclude that robotic catheter systems can improve safety of the ablation and reduce the procedure duration. Di et al. [19] prove that robotic ablation of atrial fibrillation is safe and effective. Yokoyama et al. [20] present a contact sensing catheter and investigate the relationship between contact force and the tissue temperatures, lesion size, and steam pop under blood flow. Yip et al. [3] use a low-pass filter to block the blood flow disturbances affecting the position and force measurement of the controller. Several sensor-less contact force estimation methods, employing distal shaft measurement or pose measurement based on different kinematic models of the catheter, are proposed in [21]–[23]. Razban et al. [24] propose a contact force estimation approach using contact points tracking and image-based deflection measurement. Haouchine et al. [25] use the visual feedback from stereoscopic camera for contact force estimation. In [26], the contact force, modeled by Signorini's contact model, is solved numerically as a constrained optimization problem, and a closed-loop controller regulating the contact force is designed based on finite element model of the robotic catheter.

In this study, the desired normal contact force is restricted to the range from 10 g to 25 g (0.1 N∼0.25 N), and the ability of the MRI-actuated robotic catheter to maintain the contact force in this narrow therapeutic range given LIV blood flow disturbances is investigated. Specifically, the focus is on how the blood flow disturbances will affect the contact stability and contact safety of the robotic catheter and what normal force is required to provide stable and safe contact given blood flow disturbances.

III. Pseudo-Rigid-Body Model of the Catheter

In this study, the catheter kinematics is modeled using a Pseudo-Rigid-Body (PRB) model [10], [11]. Specifically, the catheter is modeled as a series of pseudo-rigid links joined by elastic revolute joints (Fig. 2) where each joint is modeled as a spherical joint. The parametrization of the i-th joint angles of the robotic catheter is given as $\theta_i = [\theta_{ix}, \theta_{iy}, \theta_{iz}]^T$ [27]. The shape of the catheter can be described by the joint angle vector $\theta = [\theta_1^T, \theta_2^T, \ldots, \theta_n^T]^T \in \mathbf{C} \subset \mathbb{R}^{3n}$, where n is the number of the pseudo joints, $\mathbf{C}$ denotes the configuration space of the catheter robot [27].

The catheter is actuated by a set of actuators embedded on the robotic catheter [10], where each actuator contains one set of tri-axial actuation coils. The magnetic moment generated by the j-th actuator embedded on the catheter is computed as $\mu_j = n_j Z_j u_j$, where $j = 1,..,M$, and M is the number of actuators. $u_j \in \mathbb{R}^3$ denotes the actuation currents, n_j and Z_j are diagonal matrices whose diagonal elements are the number of winding turns and the cross sectional area (in body frame) of the actuation coils, respectively. Let B_j denote the static magnetic field B_s of the MRI scanner expressed

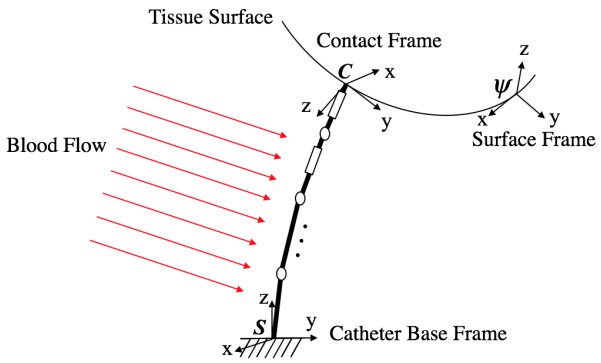

Fig. 2. The MRI-actuated robotic catheter with two sets of tri-axial actuation coils subject to the perturbation forces resulting from blood flow drag forces and the tissue surface constraint. The catheter base frame S is given as shown. Ψ denotes the surface parametrization. The contact frame C is chosen such that its origin is located at the contact point of the catheter and the z-axis is the outward normal of the tissue surface.

in the body frame of the j-th actuator. B_j is computed as $B_j = R_{sj}^T B_s$, where R_{sj}^T denotes the rotation matrix of the frame attached to the j-th actuator relative to the spatial frame [28]. The resulting Lorentz forces generated on the coils by the static magnetic field is given by $(n_j Z_j u_j)^\wedge B_j = -B_j{}^\wedge (n_j Z_j) u_j$, where $^\wedge$ is the cross product operator.

These actuation moments can then be mapped to the joint torques $\tau(\theta,u) \in \mathbb{R}^{3n}$ as [27]:

$$\tau(\theta,u) = \sum_j^M J_{su_j}^{b\ T} \begin{bmatrix} 0 \\ B_j{}^\wedge (n_j Z_j) \end{bmatrix} u_j = A(\theta)u. \qquad (1)$$

Here, $J_{su_j}^b$ is the body Jacobian corresponding to actuator j, and

$$A(\theta) = \begin{bmatrix} \ldots & J_{su_j}^{b\ T} \begin{bmatrix} 0 \\ B_j{}^\wedge (n_j Z_j) \end{bmatrix} & \ldots \end{bmatrix}, \qquad (2)$$

$j = 1,..,M$. $\tau(\theta,u)$ will be denoted as τ_u in the rest of the paper for convenience.

IV. Catheter-Surface Contact Model

A. Modeling of Blood Flow Disturbances

Periodic blood flow passing through the left atrium will exert drag forces on the catheter, as depicted in Fig. 2. Accurately modeling the blood flow inside the heart and the resulting drag forces on the catheter in their full complexity would not be computationally feasible to be used as part of a robotic catheter control scheme. The computational challenges of the blood flow modeling mainly come from the non-Newtonian properties of blood. The fluid properties of blood flow are also sensitive to temperature, hematocrit, age of red blood cells [29], etc. Therefore, in this study, a simplified blood flow drag force model will be employed. Specifically, the blood flow drag forces acting on the catheter will be modeled as probabilistic perturbation forces. The set of perturbation forces and their associated probabilities will be estimated using a quasi-steady flow model. Specifically, a distribution of blood flow velocities will be generated from a temporal sampling of the blood flow velocity profile observed

at the pulmonary veins from where the blood enters into the left atrium. Then the distribution of blood flow drag forces will be calculated using these samples of blood flow velocities, approximating the flow to be steady and uniform within the small time interval. Since the flows in the left atrium and great vessels are generally fast and dominated by inertial forces rather than viscous forces [30], the friction drag and the viscous drag can be ignored, and the pressure drag F_D applied on catheter can be calculated as [31]:

$$F_D = \frac{1}{2}\rho C_D A v^2. \tag{3}$$

Since the catheter is moved rather slowly by the physician during ablation for proper lesion formation, v is approximately the speed of the fluid. A is the projected area of the catheter on the plane orthogonal to the flow direction, C_D is the drag coefficient which is correlated to the dimensional ratio [31], and ρ is the density of the blood. The drag applied on the catheter can be expressed by the lumped drags applied on each of the catheter pseudo links as shown in Fig. 2. Based on (3), the lumped force applied on the j-th pseudo link in spatial frame is given by

$$f_b{}^j = \frac{1}{2}\rho C_{Dj} A_j v^2 w_v, \tag{4}$$

where $j = 0, 1, 2, ..., n$. A_j is the projected area of the j-th pseudo link on the plane orthogonal to the flow direction, C_{Dj} is the corresponding drag coefficient, and $w_v \in \mathbb{R}^{3x1}$ is the direction vector of the blood flow velocity in spatial frame, with $||w_v|| = 1$.

The external wrench at the i-th joint frame is given as:

$$\begin{bmatrix} f_e^i \\ \tau_e^i \end{bmatrix} = \mathrm{Ad}_{R_{si}^T} \begin{bmatrix} f_b{}^i \\ 0^{3x1} \end{bmatrix}, \ \mathrm{Ad}_{R_{si}^T} = \begin{bmatrix} R_{si}^T & 0 \\ 0 & R_{si}^T \end{bmatrix}, \tag{5}$$

where R_{si} denotes the rotational transformation of the i-th joint frame relative to the spatial frame.

The joint torques, $F_e^i(\theta,\ v)$, resulting from the external wrench acting on the i-th joint can then be calculated as:

$$F_e^i(\theta,\ v) = J_{si}^{bT}(\theta) \begin{bmatrix} f_e^i \\ \tau_e^i \end{bmatrix}, \tag{6}$$

where $J_{si}^b(\theta) \in \mathbb{R}^{6\times 3n}$ is the body Jacobian of the i-th joint [32] with

$$J_{si}^b(\theta) = [\xi_{1x}^\dagger\ \xi_{1y}^\dagger\ \xi_{1z}^\dagger\ \cdots\ \xi_{ix}^\dagger\ \xi_{iy}^\dagger\ \xi_{iz}^\dagger\ \ 0\ 0\ 0], \tag{7}$$

$$\xi_{ik}^\dagger = \mathrm{Ad}^{-1}_{(e^{\hat{\xi}_i\theta_i}\ldots e^{\hat{\xi}_n\theta_n} g_{si}(0))} \xi_{ik}(\theta_i), \tag{8}$$

where $g_{si}(0)$ is the inital configuration of the i-th joint, $\xi_{ik}(\theta_i)$ is the twist of the i-th joint in k direction, $k = x, y, z$. $\xi_{ik}(\theta_i)$ is computed as [28]:

$$\xi_{ik}(\theta_i) = \left(\frac{\partial e^{\hat{\xi}_i\theta_i}}{\partial \theta_{ik}} e^{-\hat{\xi}_i\theta_i}\right)^\vee, \tag{9}$$

$^\vee$ is the operator to extract the $\mathbb{R}^6$ vector which parameterizes a twist [33]. The total joint torque generated by the blood flow drag is then given as $F_e(\theta,\ v) = \sum_{i=1}^n F_e^i(\theta,\ v)$.

B. Contact Force and Contact Ratio

In this section, the catheter-tissue contact model based on the PRB model introduced in Section III is formulated. The origin of the contact frame is located at the contact point, and its z-axis is in the outward surface normal direction, as indicated by Fig. 2. The contact between the catheter and the tissue surface is assumed as point contact with friction (non-conforming), the contact Jacobian $J_C \in \mathbb{R}^{3\times 3n}$ relating contact forces to joint torques [33] is given by:

$$J_C = \mathbf{B}_c^T \mathrm{Ad}_{g_{sc}^{-1}} J_{st}^s, \tag{10}$$

$$\mathrm{Ad}_{g_{sc}^{-1}} = \begin{bmatrix} R_{sc}^T, & -R_{sc}^T \hat{p_{sc}} \\ 0, & R_{sc}^T \end{bmatrix}, \tag{11}$$

where the wrench basis $\mathbf{B}_c = [I^{3\times 3}, 0^{3\times 3}]^T$, R_{sc} and p_{sc} are respectively the rotational and translational transformation of the contact frame relative to spatial frame. $g_{sc} \in SE(3)$ denotes the transformation of the contact frame relative to spatial frame. J_{st}^s is the spatial manipulator Jacobian.

The friction forces between the catheter tip and the tissue surface is modeled by the Coulomb friction model. Let λ_c denote the magnitude of the normal contact force, λ_{f1} and λ_{f2} denote the tangential forces. In Coulomb friction model, the friction cone is then given as:

$$FC = \{f_c \in \mathbb{R}^3\ :\ \sqrt{{\lambda_{f1}}^2 + {\lambda_{f2}}^2} \le \mu_s \lambda_c\}, \tag{12}$$

where f_c denotes the contact force and $f_c = [\lambda_{f1}\, \lambda_{f2}\, \lambda_c]^T$, μ_s denotes the Coulomb friction coefficient [33]. The friction cone defines the set of "stable" contact forces which cause no slippage between the catheter tip and the surface.

The relationship between the catheter joint configurations and the actuation currents under joint torque F_e generated by blood flow is described by the quasi-static equilibrium[1] equation given as

$$N(\theta) + K\theta - J_C^T f_c - \tau_u - F_e = 0, \tag{13}$$

where K is the stiffness coefficient matrix, and N is the gravitational effect term. The contact force is then calculated as:

$$f_c = J_C^{T\dagger}(N(\theta) + K\theta - \tau_u - F_e). \tag{14}$$

where $J_C^{T\dagger}$ is the left pseudo-inverse of J_C^T with $J_C^{T\dagger} = (J_C J_C^T)^{-1} J_C$.

The contact ratio σ_μ between friction force and normal force is defined as:

$$\sigma_\mu = \frac{\|\lambda_f\|}{\lambda_c}, \tag{15}$$

where $\sigma_\mu \in \mathbb{R}$. Then for contact forces with $0 \le \sigma_\mu \le \mu_s$, the contact force will remain inside the friction cone FC and the catheter can sustain a stable contact with the tissue surface at the target contact position.

[1]Since the catheter moves with low velocity and acceleration during catheter ablation, the inertial and Coriolis forces are negligible, and therefore can be neglected.

V. Probabilistic Contact Stability and Contact Safety Metrics

Given blood flow velocity samples and the flow direction, the stability of the catheter's contact with the tissue surface is quantified using the probabilistic contact stability metric:

$$\kappa_\sigma = P(0 \leq \sigma_\mu \leq \mu_s), \tag{16}$$

namely, the probability that the contact force between the catheter tip and the tissue surface remains inside the friction cone FC, or equivalently, the contact ratio remains $0 \leq \sigma_\mu \leq \mu_s$, under given disturbances.

Similarly, the safety of the catheter's contact with the tissue surface is quantified using the probabilistic contact safety metric:

$$\kappa_f = P(f_{\min} \leq f_{\text{normal}} \leq f_{\max}), \tag{17}$$

namely, the probability that the normal component of the contact force between the catheter tip and the tissue surface remains inside the range $[f_{\min}, f_{\max}]$, under given disturbances.

In this paper, sample based representations are used to represent the blood flow and contact ratio probability distributions for more easily accommodating non-Gaussian probability distributions and non-linear transformations [34]. First, the samples of the blood flow velocity distribution, $\{v^{[1]}, v^{[2]}, ..., v^{[N_v]}\}$, are drawn from the blood flow velocity probability density function p_v, i.e., $v^{[j]} \sim p_v$. The corresponding contact ratio samples $\{\sigma_\mu^{[1]}, \sigma_\mu^{[2]}, ..., \sigma_\mu^{[N_v]}\}$, which represent the probability distribution of the contact ratio, p_{σ_μ}, are then obtained from $v^{[j]}$ using (4)–(15). Specifically, from (4)–(6) and (14),

$$\begin{aligned} f_c^{[j]} = -J_C^{T\dagger} \sum_{i=1}^{n} J_{si}^{bT} \mathrm{Ad}_{R_{si}^T} \begin{bmatrix} k_i w_v \\ 0^{3x1} \end{bmatrix} v^{[j]2} \\ + J_C^{T\dagger}(N(\theta) + K\theta - \tau_u), \end{aligned} \tag{18}$$

where k_i denotes the flow drag coefficient for the i-th link and $k_i = \frac{1}{2}\rho C_{Di} A_i$. The terms of (18) are grouped as:

$$f_c^{[j]} = J_{cv} v^{[j]2} + q_{cv}, \tag{19}$$

where $J_{cv}, q_{cv} \in \mathbb{R}^{3\times 1}$. (19) is then decomposed into its components (in the contact frame) as:

$$\begin{cases} f_{c1}^{[j]} = J_{cv_1} v^{[j]2} + q_{cv_1} \\ f_{c2}^{[j]} = J_{cv_2} v^{[j]2} + q_{cv_2} \\ f_{c3}^{[j]} = J_{cv_3} v^{[j]2} + q_{cv_3}. \end{cases} \tag{20}$$

where f_{c1}, f_{c2} are the tangential components of the contact force, f_{c3} is the normal component of the contact force. The corresponding contact ratio sample can then be computed as:

$$\sigma_\mu{}^{[j]} = \frac{\sqrt{f_{c1}^{[j]2} + f_{c2}^{[j]2}}}{f_{c3}^{[j]}}. \tag{21}$$

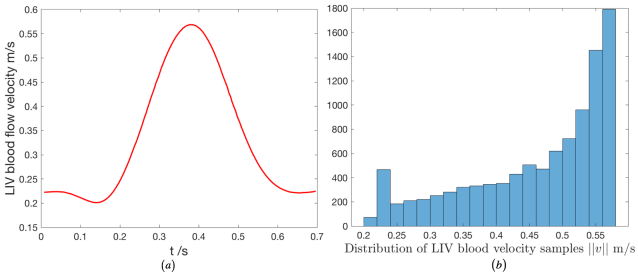

Fig. 3. (a) The left inferior pulmonary vein (LIV) blood flow velocity profile calculated from the data reported in [35] using a distal diameter of 1.8 cm. The minimum and maximum blood flow velocities are 0.21 m/s and 0.57 m/s, respectively. (b) Histogram of the 10,000 blood flow velocity samples drawn from the blood flow velocity profile in (a).

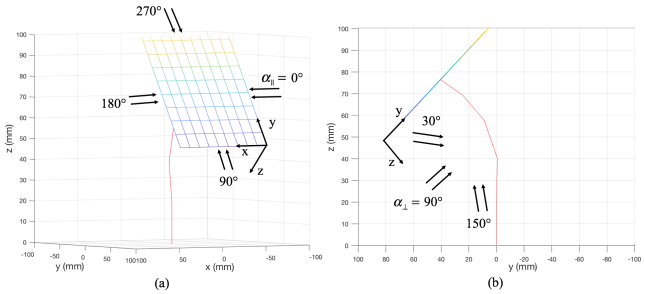

Fig. 4. (a) The illustration of the blood flow directions in the tangential plane. The directional angle $\alpha_\parallel$ is sampled in $[0°,\ 360°]$. (b) The illustration of the blood flow directions in the plane perpendicular to the tangential plane at $\alpha_\parallel{}' = 90°$. $\alpha_\perp$ is varied in $[30°,\ 150°]$. At $\alpha_\perp = 90°$, the blood flow direction is parallel to the tangential plane.

The probabilistic contact stability metric κ_σ for the given blood flow disturbance is then:

$$\kappa_\sigma = \frac{1}{N_v} \sum_{j=1}^{N_v} U_\sigma(\sigma_\mu{}^{[j]}), \tag{22}$$

where $U_\sigma(y) = 1$ if $0 \leq y \leq \mu_s$, and 0 otherwise. Analogously, the probabilistic contact safety metric κ_f for the given blood flow disturbance is given by:

$$\kappa_f = \frac{1}{N_v} \sum_{j=1}^{N_v} U_f(f_{c3}^{[j]}), \tag{23}$$

where $U_f(y) = 1$ if $f_{\min} \leq y \leq f_{\max}$, and 0 otherwise.

VI. Contact Stability and Safety Analysis — An Example Scenario

In this section, the contact stability and safety analysis performed for a sample catheter-tissue contact scenario is presented. Specifically, in the presented analysis, the effect of the nominal (disturbance-free) contact force on the stability and safety of the catheter-tissue contact under blood flow disturbances is investigated for a specific catheter-tissue contact configuration.

A. Contact Stability and Safety Analysis Scenario Setup

In this analysis scenario, we will investigate how the contact stability and safety metrics vary for three nominal normal contact force levels, namely, at 0.25 N (high), 0.20 N

(moderate) and 0.10 N (low). Additionally, we will identify the range of permissible nominal normal force levels to maintain stable and safe catheter-tissue contact.

The parameters of catheter robot model used in this paper are based on the parameters identified in [28] of our MRI-actuated robotic catheter prototype. The mechanical model of the catheter has 5 pseudo-rigid links, each with 20 mm length, for a total length of 100 mm. The outer radius of the robotic catheter is given as $r = 1.58$ mm. The blood flow density used in this paper is given as $\rho = 1.04 \times 10^3\ kg/m^3$ [36]. Since the length of each pseudo-link is equal, the drag coefficient C_D for each pseudo link is given as $C_D = 0.76$ [31]. The coefficient of friction between the robotic catheter and the atrial surface is given as $\mu_s = 0.2$ as suggested by [37].

In each case, the catheter is actuated to produce the corresponding nominal normal contact force level in the absence of disturbances using the contact force control algorithm proposed in [7].

In the analysis, a distribution obtained by sampling of the left inferior pulmonary vein[2] (LIV) blood flow is used as the underlying blood flow velocity distribution. Specifically, 10,000 velocity samples $\{v^{[i]}\}$ are drawn from the left inferior pulmonary vein blood flow velocity profile reported in [35], as shown in Fig. 3.

The blood flow direction varies substantially during the cardiac cycle. Therefore, as part of the analysis to investigate how the blood flow disturbances affect the stability and safety of the catheter-tissue contact, we have also looked at the variation of the contact stability and safety metrics for a range of blood flow directions. Specifically: Let $\alpha_{\parallel}$ denote the direction angle of the blood flow in the tangential plane of the tissue surface at the contact point, and $\alpha_{\perp}$ denote the direction angle in the plane perpendicular to the tangential plane.[3] The blood flow direction w_v in spatial frame is then given as

$$w_v = R_s[\ \sin(\alpha_{\perp})\cos(\alpha_{\parallel}) \quad \sin(\alpha_{\perp})\sin(\alpha_{\parallel}) \quad \cos(\alpha_{\perp})\ ]^T$$

, where $R_s \in SO(3)$ denotes the rotational transformation from the surface frame to the catheter spatial frame. In this study, we consider $\alpha_{\parallel} \in [0^\circ,\ 360^\circ]$ and $\alpha_{\perp} \in [30^\circ,\ 150^\circ]$, as shown in Fig. 4.

B. Analysis Results

First, the contact stability metric κ_σ, and the contact safety metric κ_f are calculated for the nominal normal contact force of 0.25 N (the upper limit of the range of normal contact forces considered safe), under the LIV blood flow disturbances for the flow directions being considered. As presented in Fig. 5 (a), the probabilistic contact stability metric κ_σ is 1 for all considered blood flow directions, indicating a stable contact between the catheter tip and tissue surface under the potential LIV blood flow disturbances. The resulting probabilistic contact safety metric κ_f under the blood flow disturbances are provided in Fig. 5 (b), where the probabilistic contact safety metric κ_f falls below 1 at some directional regions (and actually equals 0 for some directional regions), indicating unsafe catheter-tissue contact forces.

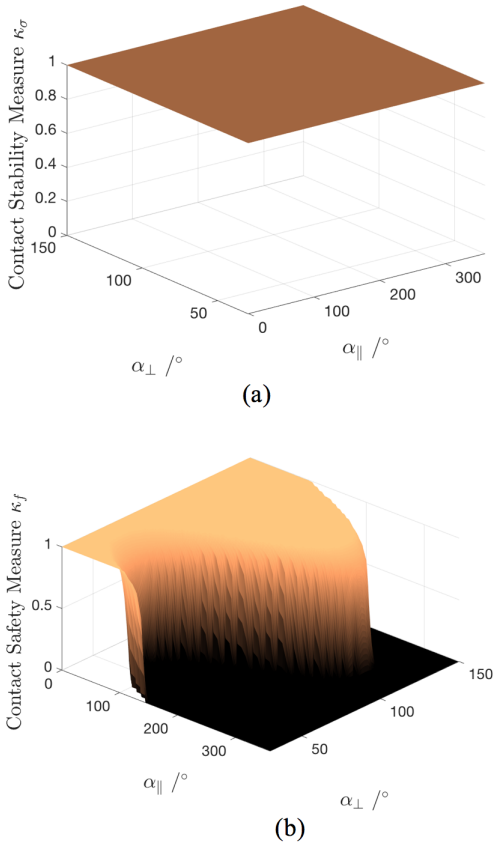

Fig. 5. Results for nominal contact normal force magnitude of 0.25 N. (a) The probabilistic contact stability metric κ_σ for blood flow directions $\alpha_{\parallel} \in [0^\circ,\ 360^\circ]$ and $\alpha_{\perp} \in [30^\circ,\ 150^\circ]$. (b) The probabilistic contact safety metric κ_f for blood flow directions $\alpha_{\parallel} \in [0^\circ,\ 360^\circ]$ and $\alpha_{\perp} \in [30^\circ,\ 150^\circ]$. The catheter-tissue contact remains stable for all blood flow directions, but, contact forces can fall outside the specified limits for some blood flow directions.

In the next case, the contact stability and safety metrics κ_σ and κ_f are calculated for the moderate nominal normal contact force (0.2 N). As shown in Fig. 6 (a) and (b), both the contact stability and the contact safety metrics are equal to 1 for all considered blood flow directions, indicating stable contact with contact forces within the safe limits.

The lower force limit of 0.1 N is then tested under the LIV blood flow disturbances. The resulting probabilistic contact stability metrics and contact safety metrics over different flow directions are presented in Fig. 7 (a) and (b), respectively. As shown in Fig. 7 (a), with normal force of 0.1 N, the robotic catheter can still provide a stable catheter-tissue contact over the considered blood flow directions. However, the external joint torque created by the blood flow disturbances in some directional regions can lead to a normal force lower than the force limit of 0.1 N, pushing

[2]Left inferior pulmonary vein is one of the four pulmonary veins connected to the left atrium and is targeted in the pulmonary vein isolation technique of the atrial fibrillation ablation procedure.

[3]$\alpha_{\parallel}$ and $\alpha_{\perp}$ can be thought as the azimuth and elevation angles for the blood flow direction relative to the tissue tangent surface at the catheter tip.

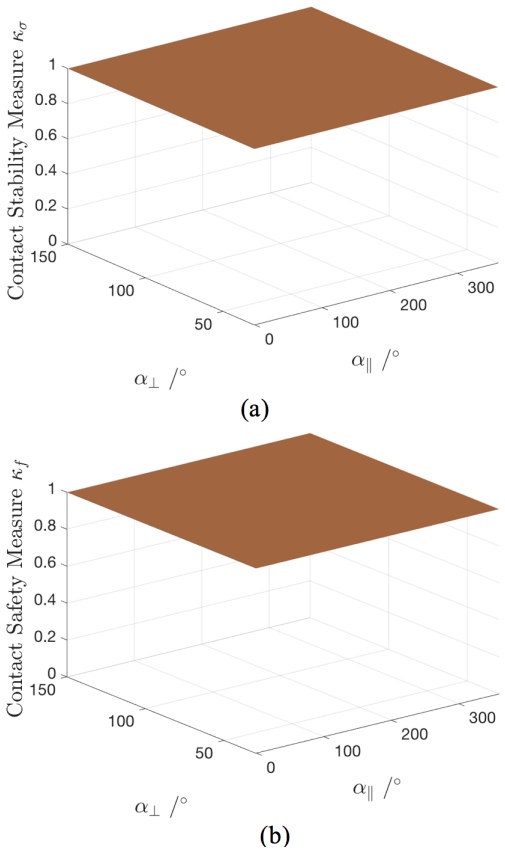

Fig. 6. Results for nominal contact normal force magnitude of 0.2 N. (a) The probabilistic contact stability metric κ_σ for blood flow directions $\alpha_\parallel \in [0°,\ 360°]$ and $\alpha_\perp \in [30°,\ 150°]$. (b) The probabilistic contact safety metric κ_f for blood flow directions $\alpha_\parallel \in [0°,\ 360°]$ and $\alpha_\perp \in [30°,\ 150°]$. The catheter-tissue contact remains stable and within specified contact force limits for all blood flow directions.

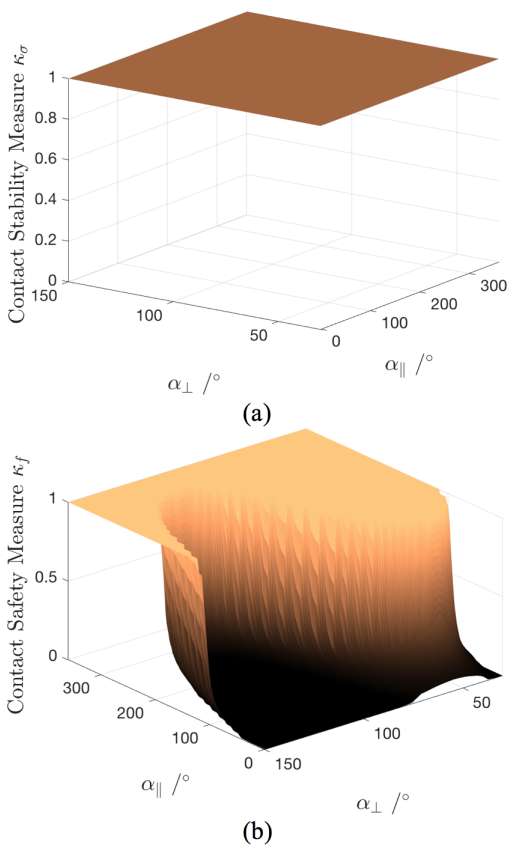

Fig. 7. Results for nominal contact normal force magnitude of 0.1 N. (a) The probabilistic contact stability metric κ_σ for blood flow directions $\alpha_\parallel \in [0°,\ 360°]$ and $\alpha_\perp \in [30°,\ 150°]$. (b) The probabilistic contact safety metric κ_f for blood flow directions $\alpha_\parallel \in [0°,\ 360°]$ and $\alpha_\perp \in [30°,\ 150°]$. The catheter-tissue contact remains stable for all blood flow directions, but, contact forces can fall outside the specified limits for some blood flow directions.

the probabilistic contact safety metric κ_f below 1, as shown in Fig. 7 (b).

Finally, a catheter configuration under a low normal force of 0.09 N is evaluated. The resulting probabilistic contact stability and contact safety metrics with respect to the experimented flow directions are presented in Fig. 8. As shown in Fig. 8 (a), potential slippage between the catheter tip and tissue surface may occur for some blood flow directions, as the probabilistic contact stability metric $\kappa_\sigma < 1$. At this level of nominal normal force, normal forces can fall outside the specified limits for all flow directions, as the contact safety metric never reaches to 1 for any of the flow directions.

The simulation results presented in Fig. 5-7 show that the catheter-tissue contact stability can be guaranteed with nominal normal contact forces from 0.1 N to 0.25 N; however, the blood flow disturbances can push the normal force out of the desired force limits when the given normal force approaches to the upper and lower force limits. A further analysis performed by varying the nominal normal contact forces and identifying the range of contact forces that achieve $\kappa_\sigma \equiv 1$ and $\kappa_f \equiv 1$, reveal that a minimum nominal normal force of 0.12 N and maximum nominal normal force of 0.23 N should be applied by the robotic catheter in order to maintain stable and safe contact under the LIV blood flow disturbances for the range of flow directions considered. The distributions of the resulting normal forces under different LIV blood flow directions for given nominal normal forces of 0.12 N and 0.23 N are presented in Fig. 9.

In Fig. 9 (a) and (b) the distribution of the resulting normal forces is presented when the LIV blood flow direction is varied for the nominal normal contact force of 0.12 N. First, in Fig. 9 (a), the flow direction is varied in the tangential plane ($\alpha_\perp = 0°$) to identify the worst case tangential blood flow direction, which occurs at $\alpha_\parallel = 104°$. Then, in Fig. 9 (b), the blood flow direction is varied in the perpendicular plane for this particular tangential flow direction ($\alpha_\parallel = 104°$), where it can be observed that the force distribution range reaches the lower bound of the safe normal force range (0.1 N) at $\alpha_\perp = 112°$. Similarly, in Fig. 9 (c) and (d), the histogram of the resulting normal forces under the LIV blood flow perturbations is presented for the nominal normal contact force of 0.23 N. In this case, the worst case tangential flow direction is observed to be at $\alpha_\parallel = 281°$ (Fig. 9-c), and the force distribution range reaches the upper bound of the safe normal force range (0.25 N) at $\alpha_\perp = 66°$ (Fig. 9-d).

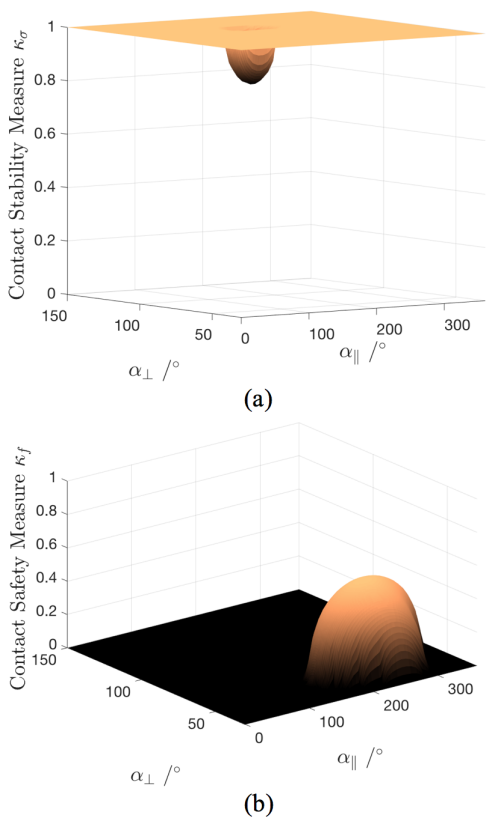

Fig. 8. Results for nominal contact normal force magnitude of 0.09 N. (a) The probabilistic contact stability metric κ_σ for blood flow directions $\alpha_\parallel \in [0^\circ,\ 360^\circ]$ and $\alpha_\perp \in [30^\circ,\ 150^\circ]$. (b) The probabilistic contact safety metric κ_f for blood flow directions $\alpha_\parallel \in [0^\circ,\ 360^\circ]$ and $\alpha_\perp \in [30^\circ,\ 150^\circ]$. The catheter-tissue contact may lead to slippage for some blood flow directions as there are regions of flow directions where the probability of stable contact drops below 1; Contact forces can fall outside the specified limits for all flow directions, since contact safety metric never reaches to 1 for any of the flow directions.

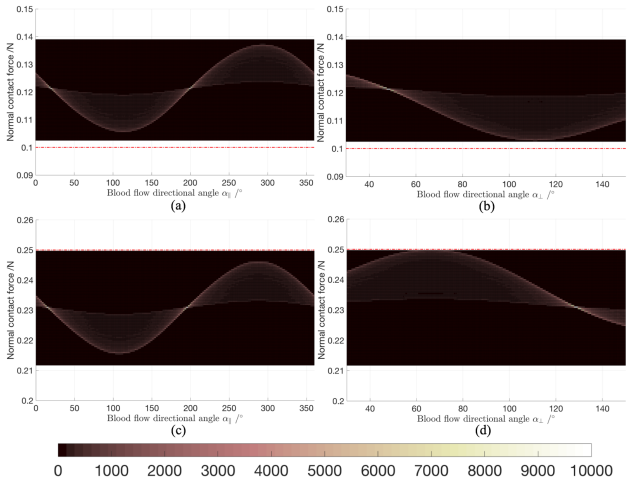

Fig. 9. (a) The histogram of the resulting normal contact forces when the LIV blood flow direction is varied in the tangential plane ($\alpha_\parallel \in [0^\circ,\ 360^\circ]$, with $\alpha_\perp = 0^\circ$), for a nominal normal contact force of 0.12 N. The lowest resulting normal contact force occurs at $\alpha_\parallel = 104^\circ$. (b) The histogram of the resulting normal contact forces when the blood flow is varied in the perpendicular plane ($\alpha_\perp \in [30^\circ,\ 150^\circ]$) for $\alpha_\parallel = 104^\circ$. (c) The histogram of the resulting normal contact forces when the LIV blood flow direction is varied in the tangential plane ($\alpha_\parallel \in [0^\circ,\ 360^\circ]$, with $\alpha_\perp = 0^\circ$), for a nominal normal contact force of 0.23 N. The highest resulting normal contact force occurs at $\alpha_\parallel = 281^\circ$. (b) The histogram of the resulting normal contact forces when the blood flow is varied in the perpendicular plane ($\alpha_\perp \in [30^\circ,\ 150^\circ]$) for $\alpha_\parallel = 281^\circ$.

VII. Conclusion

Understanding and analyzing the effects of blood flow disturbances on stability and safety of catheter-tissue contact is critical for development of robotic intravascular cardiac catheter systems. In this paper, a probabilistic blood flow disturbance model is introduced. In the proposed model, the blood flow drag forces applied on the catheter body are approximated using a quasi-static model. Building on this blood flow disturbance model, probabilistic contact stability and contact safety metrics, which employ a sample based representation of the blood flow velocity distribution, are defined. The proposed models and metrics are then employed in an example scenario to analyze the catheter-tissue contact stability and safety for a MRI-actuated robotic catheter in a specific catheter-tissue contact configuration. The simulation results show that the blood flow disturbances can greatly affect the contact stability and contact safety of the MRI-actuated robotic catheter.

Experimental validation of the proposed models and the analysis framework is the natural next step for the presented research. The contact analysis results provided by the proposed models and methods will be experimentally validated using a prototype of our MRI-actuated robotic catheter system as part of our subsequent research.

Although MRI-actuated robotic catheter system being developed by the investigators was considered as the underlying example robotic catheter platform throughout the paper, the proposed models and methods are broadly applicable to other types of robotic catheters.

The presented formulation explicitly used a PRB model of the catheter mechanics when deriving blood flow disturbances and catheter-surface contact models (Section IV). However, the formulation does not rely on any specific inherent property of the PRB model, and hence can be generalized to other types of models for catheter mechanics, as long as appropriate Jacobians are available. Generalization of the formulation to other types of catheter models will be the subject of our future work.

References

[1] P. Chowdhury, W. R. Lewis, R. A. Schweikert, and J. E. Cummings, "Ablation of atrial fibrillation: What can we tell our patients?" *Cleveland Clinic Journal of Medicine*, vol. 76, no. 9, pp. 543–550, 2009.

[2] S. G. Yuen, M. C. Yip, N. V. Vasilyev, D. P. Perrin, J. Pedro, and R. D. Howe, "Robotic force stabilization for beating heart intracardiac surgery," in *International Conference on Medical Image Computing and Computer-Assisted Intervention*. Springer, 2009, pp. 26–33.

[3] M. C. Yip, J. A. Sganga, and D. B. Camarillo, "Autonomous control of continuum robot manipulators for complex cardiac ablation tasks," *Journal of Medical Robotics Research*, vol. 2, no. 01, p. 1750002, 2017.

[4] S. B. Kesner and R. D. Howe, "Robotic catheter cardiac ablation combining ultrasound guidance and force control," *The International Journal of Robotics Research*, vol. 33, no. 4, pp. 631–644, 2014.

[5] O. Bebek and M. C. Cavusoglu, "Intelligent control algorithms for robotic-assisted beating heart surgery," *IEEE Transactions on Robotics*, vol. 23, no. 3, pp. 468–480, 2007.

[6] S. G. Yuen, S. B. Kesner, N. V. Vasilyev, P. J. Del Nido, and R. D. Howe, "3d ultrasound-guided motion compensation system for beating heart mitral valve repair," in *International Conference on Medical Image Computing and Computer-Assisted Intervention*. Springer, 2008, pp. 711–719.

[7] R. Hao, T. Greigarn, and M. C. Çavuşoğlu, "Contact stability analysis of magnetically-actuated robotic catheter under surface motion," in *IEEE International Conference on Robotics and Automation*, 2020.

[8] T. Liu and M. C. Çavuşoğlu, "Three dimensional modeling of an mri actuated steerable catheter system," in *Robotics and Automation (ICRA), 2014 IEEE International Conference on*. IEEE, 2014, pp. 4393–4398.

[9] T. Liu, N. L. Poirot, D. Franson, N. Seiberlich, M. A. Griswold, and M. C. Cavusoglu, "Modeling and validation of the three-dimensional deflection of an mri-compatible magnetically actuated steerable catheter." *IEEE Trans. Biomed. Engineering*, vol. 63, no. 10, pp. 2142–2154, 2016.

[10] T. Greigarn and M. C. Çavuşoğlu, "Pseudo-rigid-body model and kinematic analysis of mri-actuated catheters," in *Robotics and Automation (ICRA), 2015 IEEE International Conference on*. IEEE, 2015, pp. 2236–2243.

[11] M. Khoshnam and R. V. Patel, "A pseudo-rigid-body 3r model for a steerable ablation catheter," in *2013 IEEE International Conference on Robotics and Automation*. IEEE, 2013, pp. 4427–4432.

[12] V. Y. Reddy, D. Shah, J. Kautzner, B. Schmidt, N. Saoudi, C. Herrera, P. Jaïs, G. Hindricks, P. Peichl, A. Yulzari *et al.*, "The relationship between contact force and clinical outcome during radiofrequency catheter ablation of atrial fibrillation in the toccata study," *Heart rhythm*, vol. 9, no. 11, pp. 1789–1795, 2012.

[13] J. G. Andrade, G. Monir, S. J. Pollak, P. Khairy, M. Dubuc, D. Roy, M. Talajic, M. Deyell, L. Rivard, B. Thibault *et al.*, "Pulmonary vein isolation using "contact force" ablation: the effect on dormant conduction and long-term freedom from recurrent atrial fibrillation—a prospective study," *Heart Rhythm*, vol. 11, no. 11, pp. 1919–1924, 2014.

[14] R. Wakili, S. Clauss, V. Schmidt, M. Ulbrich, A. Hahnefeld, F. Schüssler, J. Siebermair, S. Kääb, and H. L. Estner, "Impact of real-time contact force and impedance measurement in pulmonary vein isolation procedures for treatment of atrial fibrillation," *Clinical Research in Cardiology*, vol. 103, no. 2, pp. 97–106, 2014.

[15] A. Pedrote, J. Acosta, B. Jauregui-Garrido, M. Frutos-Lopez, and E. Arana-Rueda, "Paroxysmal atrial fibrillation ablation: Achieving permanent pulmonary vein isolation by point-by-point radiofrequency lesions," *World journal of cardiology*, vol. 9, no. 3, p. 230, 2017.

[16] A. Thiagalingam, A. D'AVILA, L. Foley, J. L. Guerrero, H. Lambert, G. Leo, J. N. Ruskin, and V. Y. Reddy, "Importance of catheter contact force during irrigated radiofrequency ablation: evaluation in a porcine ex vivo model using a force-sensing catheter," *Journal of cardiovascular electrophysiology*, vol. 21, no. 7, pp. 806–811, 2010.

[17] C. Sohns, R. Karim, J. Harrison, A. Arujuna, N. Linton, R. Sennett, H. Lambert, G. Leo, S. Williams, R. Razavi *et al.*, "Quantitative magnetic resonance imaging analysis of the relationship between contact force and left atrial scar formation after catheter ablation of atrial fibrillation," *Journal of cardiovascular electrophysiology*, vol. 25, no. 2, pp. 138–145, 2014.

[18] J. Dewire and H. Calkins, "State-of-the-art and emerging technologies for atrial fibrillation ablation," *Nature Reviews Cardiology*, vol. 7, no. 3, p. 129, 2010.

[19] L. Di Biase, Y. Wang, R. Horton, G. J. Gallinghouse, P. Mohanty, J. Sanchez, D. Patel, M. Dare, R. Canby, L. D. Price *et al.*, "Ablation of atrial fibrillation utilizing robotic catheter navigation in comparison to manual navigation and ablation: Single-center experience," *Journal of cardiovascular electrophysiology*, vol. 20, no. 12, pp. 1328–1335, 2009.

[20] K. Yokoyama, H. Nakagawa, D. C. Shah, H. Lambert, G. Leo, N. Aeby, A. Ikeda, J. V. Pitha, T. Sharma, R. Lazzara *et al.*, "Novel contact force sensor incorporated in irrigated radiofrequency ablation catheter predicts lesion size and incidence of steam pop and thrombus," *Circulation: Arrhythmia and Electrophysiology*, vol. 1, no. 5, pp. 354–362, 2008.

[21] M. Khoshnam, A. C. Skanes, and R. V. Patel, "Modeling and estimation of tip contact force for steerable ablation catheters," *IEEE Transactions on Biomedical Engineering*, vol. 62, no. 5, pp. 1404–1415, 2015.

[22] S. Hasanzadeh and F. Janabi-Sharifi, "Model-based force estimation for intracardiac catheters," *IEEE/ASME Transactions on Mechatronics*, vol. 21, no. 1, pp. 154–162, 2015.

[23] J. Back, T. Manwell, R. Karim, K. Rhode, K. Althoefer, and H. Liu, "Catheter contact force estimation from shape detection using a real-time cosserat rod model," in *2015 IEEE/RSJ International Conference on Intelligent Robots and Systems (IROS)*. IEEE, 2015, pp. 2037–2042.

[24] M. Razban, J. Dargahi, and B. Boulet, "A sensor-less catheter contact force estimation approach in endovascular intervention procedures," in *2018 IEEE/RSJ International Conference on Intelligent Robots and Systems (IROS)*. IEEE, 2018, pp. 2100–2106.

[25] N. Haouchine, W. Kuang, S. Cotin, and M. Yip, "Vision-based force feedback estimation for robot-assisted surgery using instrument-constrained biomechanical three-dimensional maps," *IEEE Robotics and Automation Letters*, vol. 3, no. 3, pp. 2160–2165, 2018.

[26] Z. Zhang, J. Dequidt, J. Back, H. Liu, and C. Duriez, "Motion control of cable-driven continuum catheter robot through contacts," *IEEE Robotics and Automation Letters*, vol. 4, no. 2, pp. 1852–1859, 2019.

[27] T. Greigarn, N. L. Poirot, X. Xu, and M. C. Cavusoglu, "Jacobian-based task-space motion planning for mri-actuated continuum robots," *IEEE Robotics and Automation Letters*, 2018.

[28] T. Greigarn, "Kinematics, planning, and perception for magnetically-actuated MRI-guided continuum robots," Ph.D. dissertation, Case Western Reserve University, 2018.

[29] N. Bessonov, A. Sequeira, S. Simakov, Y. Vassilevskii, and V. Volpert, "Methods of blood flow modelling," *Mathematical modelling of natural phenomena*, vol. 11, no. 1, pp. 1–25, 2016.

[30] D. N. Ku, "Blood flow in arteries," *Annual review of fluid mechanics*, vol. 29, no. 1, pp. 399–434, 1997.

[31] Y. Nakayama, *Introduction to fluid mechanics*. Butterworth-Heinemann, 2018.

[32] T. Greigarn, R. Jackson, T. Liu, and M. C. Çavuşoğlu, "Experimental validation of the pseudo-rigid-body model of the mri-actuated catheter," in *Robotics and Automation (ICRA), 2017 IEEE International Conference on*. IEEE, 2017, pp. 3600–3605.

[33] R. M. Murray, *A mathematical introduction to robotic manipulation*. CRC press, 2017.

[34] S. Thrun, W. Burgard, and D. Fox, *Probabilistic robotics*. MIT press, 2005.

[35] M. U. Qureshi, G. D. Vaughan, C. Sainsbury, M. Johnson, C. S. Peskin, M. S. Olufsen, and N. Hill, "Numerical simulation of blood flow and pressure drop in the pulmonary arterial and venous circulation," *Biomechanics and modeling in mechanobiology*, vol. 13, no. 5, pp. 1137–1154, 2014.

[36] J. Cameron, J. Skofronick, and R. Grant, *Physics of the Body*, ser. Medical Physics Series. Medical Physics Pub., 1999.

[37] T. Liu, N. Poirot, T. Greigarn, and M. Cavusoglu, "Design of an MRI-guided magnetically-actuated steerable catheter," *ASME Journal of Medical Devices, Special Issue on Cardiovascular Device Development and Safety Assessment using Computational and/or Experimental Approaches*, vol. 11, 2017.